THE JOURNAL OF PHYSICAL CHEMISTRY C

Article

pubs.acs.org/JPCC

Characterization of Photocurrent Generation Dynamics in Polymer Solar Cells Based on ZnO/CdS-Core/Shell Nanoarrays by Intensity Modulated Photocurrent Spectroscopy: Theoretical Modeling

Changwen Liu,[†] Zeliang Qiu,[†] Wenjin Yue,[†,‡] Xun Zhou,[†] and Mingtai Wang*[,†]

[†]Institute of Plasma Physics and Key Lab of Novel Thin Film Solar Cells, Chinese Academy of Sciences, Hefei 230031, People's Republic of China

[‡]School of Biochemical Engineering, Anhui Polytechnic University, Wuhu, 241000, People's Republic of China

Supporting Information

ABSTRACT: A theoretical model is developed for the dynamic characterization of hybrid polymer-based solar cells (HPSCs) based on vertically aligned ZnO/CdS-core/shell nanorod arrays (ZC-NAs) by intensity modulated photocurrent spectroscopy (IMPS). The model describes the effects of CdS shell formation on charge generation and transport dynamics. Particularly, an analytical expression for the ineffective polymer phase model in nanoarray solar cells is developed and introduced into IMPS model for the first time. The main expectations of the IMPS model are confirmed by the experimental data of the polymer/ZC-NA cells with the CdS shell thickness (L) of 3−8 nm. It is shown that the contributions from CdS absorption (f_1) and polymer absorption (f_2) to charge generation are determined by the core/shell nanoarray structure and the intrinsic polymer property, while the optimal CdS shell thickness (L_{opt}) depends on the interspacing between ZnO core nanorods and the exciton diffusion length of the polymer. The photocurrent generation is dominantly the competitive results of f_1 and f_2 contributions subjected to the change in L, with the polymer as a dominant absorption material. Fittings of the measured IMPS responses to the IMPS model reveal that the L-dependence of photocurrent generation dominantly originates from f_1, f_2, and the polymer exciton dissociation rate S at the polymer/CdS interface. Moreover, the first-order rate constants for the surface defects to trap and detrap the injected electrons in ZnO core nanorods are found to decrease with CdS shell growth and become saturated at L_{opt}. Furthermore, it is demonstrated that the effective electron diffusion coefficient D_e in the ZnO nanorods reaches a peak value at L_{opt} as the result of the largest photogenerated electron density in conduction band. Those results provide a guide to the design of efficient HPSCs based on the core/shell nanoarrays with complementary properties.

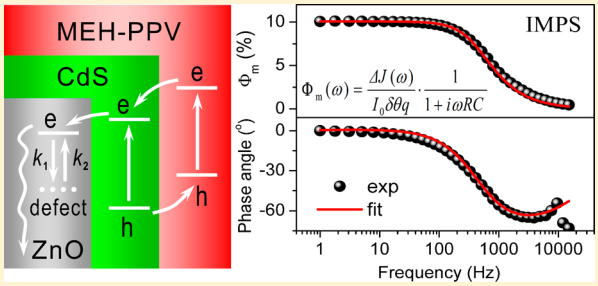

1. INTRODUCTION

Hybrid polymer-based solar cells (HPSCs) that combine conjugated polymer as the electron donor (D) with semiconductor nanocrystals as the electron acceptor (A) have received great attention due to their attractive advantages, such as low cost and easy processability.[1,2] HPSCs normally adopt a bulk-heterojunction (BHJ) architecture in which a large D/A interface area in the photoactive layer is created for the exciton dissociation into free charge carriers and the issues due to the limited exciton diffusion length (L_D) of common conjugated polymers are addressed by formation of a bicontinuous interpenetrating network of D and A phases.[3−5] Ideal BHJ devices can be produced by using vertically aligned one-dimensional (1-D) inorganic nanostructure arrays instead of the disordered A phase channels formed by individual nanoparticles dispersed in a conjugated polymer matrix.[6,7] Such an aligned BHJ structure has extraordinary advantages such as the stabilized spatial distribution of the D/A interfaces with a high area for exciton dissociation, the straightforward nanochannels for electron transport with reduced charge recombination, and the low reflectance due to light scattering and trapping.[8] Due to nontoxicity, high electron mobility, and facile synthesis at low temperature, ZnO nanorod/nanowire arrays (ZnO-NAs) have been widely used to prepare HPSCs.[9−11] However, the overall performance of polymer/ZnO-NA devices is not satisfying yet, with the mostly reported power conversion efficiencies (η) between 0.2−0.5%.[10−15]

Growth of a shell layer on the ZnO nanorods in ZnO-NAs to form core/shell nanoarrays is an effective way to improve the performance of polymer/ZnO-NA devices.[16−18] Recently, we prepared ZnO/CdS-core/shell nanoarray (ZC-NA) by depositing polycrystalline CdS shell onto the ZnO nanorod in ZnO-NA, and infiltrated poly(1-methoxy-4-(2-ethylhexyloxy)-*p*-phenylenevinylene) (MEH-PPV) into the ZC-NA to fabricate MEH-PPV/ZC-NA solar cells.[18] The device configuration and charge transfer processes in the MEH-PPV/ZC-NA devices are

Received: September 16, 2014
Revised: November 13, 2014
Published: November 25, 2014

   dx.doi.org/10.1021/jp509369n | J. Phys. Chem. C 2014, 118, 28462−28473

depicted in Figure 1. In MEH-PPV/ZC-NA devices, both polymer and CdS absorb photons for exciton generation. As the

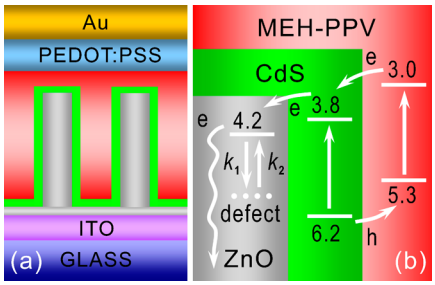

Figure 1. (a) Architecture in MEH-PPV/ZC-NA solar cells. (b) Band level (eV) alignments in the solar cells, where the arrows show the charge transfer of electrons and holes. Surface defects on ZnO nanorods can influence electron transport by trapping (k_1) and detrapping (k_2) processes. Note, when the CdS shell layer is removed, the architecture and the charge transport processes are actually for the polymer/ZnO-NA devices.

binding energy of excitons in CdS is about 180 meV,[19] much larger than the thermal energy at ambient temperature ($k_BT \sim$ 26 meV, where k_B is the Boltzmann constant and T is the temperature), the excitons generated by CdS absorption need to dissociate at the CdS/ZnO interface after diffusion rather than take a bulk dissociation inside the CdS layer. The band level alignments (Figure 1b) between MEH-PPV and CdS are favorable to the electron transfer from MEH-PPV to CdS, as confirmed by the significantly quenched photoluminescence (PL) of MEH-PPV when the polymer is incorporated into the ZC-NAs.[18] Moreover, the alignments are also favorable to the hole transfer from CdS to MEH-PPV, similar to that from CdSe or CdS quantum dots to organic dye molecules.[20,21] Therefore, the excitons generated in the polymer phase dissociate at the polymer/CdS interface by injecting electrons into CdS and further into ZnO, with holes remaining in the polymer, the excitons generated in CdS dissociate at the CdS/ZnO interface by injecting electrons into ZnO with holes injected into the polymer, and all of the photogenerated electrons are eventually transported toward the collection electrode (i.e., ITO) by ZnO-NA for photocurrent generation. In comparison to the counterpart solar cells based on ZnO-NA, the MEH-PPV/ZC-NA devices exhibit a significantly increased open-circuit voltage (V_{oc}) resulted from the passivation of the surface defects on ZnO nanorods by CdS shell formation and also a remarkably improved short-circuit current (J_{sc}) due to the supplementary light absorption of CdS.[18] Our results clearly indicated that application of core/shell structured nanoarrays with complementary properties (e.g., defect passivation and supplementary light harvesting) is promising for fabricating efficient HPSCs. However, the mechanistic understanding of the shell effects on the charge generation and transport dynamics for photocurrent generation in photovoltaic processes, which is crucially important for the optimization of device performance, is still a challenging issue.[22−25]

Intensity modulated photocurrent spectroscopy (IMPS), a powerful tool for investigation of charge generation and transport dynamics, is a kind of dynamic photoelectrochemical method and has been successfully used in dye-sensitized solar cells (DSCs)[26−28] and HPSCs.[29−31] IMPS mainly provides the periodic response of photocurrent to a small sinusoidal light perturbation ($I_{ac} = I_0\delta e^{i\omega t}$) under short-circuit condition, where I_0 is the steady-state background light intensity, δ is the modulation depth, and $\omega = 2\pi f$ is the variable modulation frequency. We have established an IMPS model for polymer/ZnO-NA devices by considering key photovoltaic steps and device architecture, and got insight into the charge generation and transport dynamics affected by ZnO nanorod length.[31] However, the previous model cannot be applied directly to polymer/ZC-NA devices. First, in the polymer/ZnO-NA devices, photogenerated excitons only come from the polymer absorption, and the invariant interspacing between ZnO nanorods leads to an unchanged exciton population in the polymer phase between the ZnO nanorods in a given illumination depth; in contrast, in the polymer/ZC-NA devices, both polymer and CdS absorption contribute to exciton generation between ZnO core nanorods, which will depend strongly on CdS shell thickness (L) in a given illumination depth. Moreover, in the polymer/ZC-NA devices, the inorganic CdS shell serves as an additional photon absorber and its absorption and excitonic properties are significantly different from that of the polymer. Thereby, the exciton generation and dissociation in polymer/ZC-NA devices are much more complicate than in polymer/ZnO-NA devices, and the previous IMPS model is not able to provide a complete description for polymer/ZC-NA devices.

In this paper, we develop an IMPS model for the HPSCs based on polymer and core/shell nanorod arrays, in which the exciton and charge generation from both polymer and shell absorption and the shell effects on electron transport dynamics are fully considered. Experimental IMPS responses of MEH-PPV/ZC-NA devices are satisfactorily fitted to the analytical expression of the model, providing new insight into the structure-related electron transport dynamics and device performance therein.

2. EXPERIMENTAL SECTION

As described previously,[18] the ZC-NAs with the CdS shell thickness of L = 3−8 nm were synthesized by using successive ion layer adsorption and reaction (SILAR) technique with ZnO-NA on ITO substrate as template, and the MEH-PPV/ZC-NA devices with Au as counter electrode with area of 3 × 3 mm^2 were fabricated. Results showed that the CdS layer was continuously formed on ZnO nanorod even though the CdS layer thickness was quite small.[18] Steady-state current−voltage ($J-V$) curves, dynamic IMPS, and intensity modulated photovoltage spectroscopy (IMVS) spectra of solar cells were measured with a controlled intensity modulated photo spectroscopy (CIMPS; Zahner Co., Germany) in ambient conditions,[31] in which the incident monochromatic light intensity (I_0 = 15.85 mW/cm^2) was illuminated on the solar cells through ITO side by a blue light-emitting diode (LED) (BLL01, λ_{max} = 470 nm, spectral half-width = 25 nm, Zahner Co.). In the dynamic measurements, the small sinusoidal perturbation $I_{ac} = I_0\delta e^{i\omega t}$ was applied in the frequency range from 1 Hz to 15 kHz with a modulation depth of δ = 0.10. During the steady and dynamic measurements, the illumination was limited to the overlapped area (3 × 3 mm^2) between ITO and Au by a photomask attached to each device.

3. THEORY

Following our previous method,[31] the core/shell nanorods are assumed to be in a shape of hexagonal prism with a flat top, and aligned vertically and hexagonally on the dense layer. Given the

dx.doi.org/10.1021/jp509369n | J. Phys. Chem. C 2014, 118, 28462−28473

core nanorods have an average radius r and interspacing l, and the shell layers have a thickness L, a unit cell is defined by two core/shell nanorods and covers the ITO substrate surface within the triangle area ΔABC with an area of $(\sqrt{3}(l + 2r)^2)/12$, as depicted in Figure 2a. The IMPS model is developed on

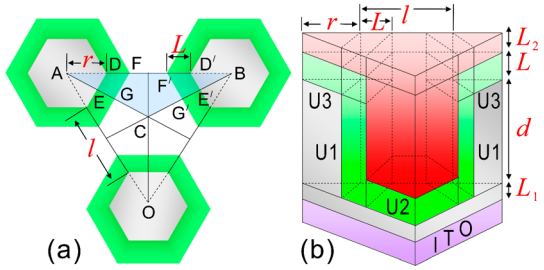

Figure 2. (a) Top view of CdS/ZnO-core/shell nanoarray on ITO substrate. (b) Unit cell for the model, where only the ZnO nanorod side face at U1 location is considered for exiton dissociation as the result of ignorable contributions from other faces provided by the ZnO nanorod top face and the dense ZnO layer. The red part between nanorods represents the polymer.

the basis of the characteristic dimensions in the unit cell shown in Figure 2b, where d is the core nanorod length, L_1 is the thickness of the ZnO dense layer for ZnO nanorod growth, and L_2 is the thickness of the polymer layer over nanorods. Therefore, three kinds of interfaces in the unit cell exist at three kinds of locations (Figure 2b). One kind of interfaces is at the U1 location that originates from the side face of a core/shell nanorod, the second kind of interfaces is at the U2 location over the ITO layer between two core/shell nanorods, and the third kind of interfaces is at the U3 location that exists on the top face of a core/shell nanorod. Clearly, each of the three kinds of locations (U1, U2, and U3) involves both CdS/ZnO and polymer/CdS interfaces. For a convenient discussion, CdS/ZnO and polymer/CdS interfaces are here classified by their locations. For instance, CdS/ZnO and polymer/CdS interfaces appearing at the U1 location are referred to as CdS/ZnO-U1 and polymer/CdS-U1 interfaces, respectively. Accordingly, there also exist in a unit cell the CdS/ZnO-U2 and polymer/CdS-U2 interfaces at the U2 location, as well as the CdS/ZnO-U3 and polymer/CdS-U3 interfaces at the U3 location.

Calculations by using the IMPS model for MEH-PPV/ZnO-NA devices[31] showed that the photocurrent generation in the aligned devices dominantly correlates with the charge generation at the MEH-PPV/ZnO interfaces formed by the ZnO nanorod side faces (Figures S1 and S2 in Supporting Information). Accordingly, for simplicity, here we only consider the photocurrent generation $\Delta J_1(\omega)$ from the interfaces at the U1 location in the unit cell of MEH-PPV/ZC-NA devices, by ignoring the charge generations from the interfaces at the U2 and U3 locations (i.e., $\Delta J_2(\omega) = 0$ for the interfaces at the U2 location, and $\Delta J_3(\omega) = 0$ for the interfaces at the U3 location). According to the CdS/ZnO-U1 and MEH-PPV/CdS-U1 interfaces from one ZnO/CdS-core/shell nanorod, there are actually two subdevices in a tandem structure at the U1 location during photocurrent generation, that is, the CdS/ZnO-NA-U1 subdevice with CdS shell serving as donor and ZnO nanorod as acceptor generates the photocurrent $\Delta j_{11}(\omega)$ on the ITO area of $S_1 = \sqrt{3}r^2/8$ (i.e., within ΔADE), and the MEH-PPV/CdS-ZnO-NA-U1 subdevice with MEH-PPV as donor and ZnO/CdS-core/shell nanorod as acceptor generates the photocurrent $\Delta j_{12}(\omega)$ on the ITO areas of $2S_1 = \sqrt{3}r^2/4$ (i.e., within ΔADE + ΔBD′E′). Note, $\Delta J_1(\omega) = 2\Delta j_{11}(\omega) + \Delta j_{12}(\omega)$ is the combined contribution from the subdevices defined by the interfaces at the U1 locations within the ITO areas of $\sqrt{3}r^2/4$ (i.e., within ΔADE + ΔBD′E′) in a unit cell. Therefore, the total *ac* photocurrent density $\Delta J(\omega)$ generated by a unit cell is the weighted average of the photocurrent densities [i.e., $\Delta J_1(\omega)$, $\Delta J_2(\omega)$, and $\Delta J_3(\omega)$] from the subdevices defined by the interfaces at the U1, U2, and U3 locations (Figure S3 in Supporting Information) when given $\Delta J_2(\omega) = \Delta J_3(\omega) = 0$.

It is a fact that the CdS and MEH-PPV absorptions in the unit cell are changed with increasing L. Hence, the contributions of the CdS/ZnO-NA-U1 and MEH-PPV/CdS-ZnO-NA-U1 subdevices to photocurrent generation in the unit cell must correlate with the L value. Since the CdS exciton diffusion length is on a centimeter scale,[32] all of the excitons generated in the CdS with a L on nanometer scale can diffuse to the CdS/ZnO interface for dissociation and thereby contribute effectively to photocurrent generation. Moreover, the population of the effective excitons in CdS shell layer increases with increasing L according to the Bouguer−Lambert−Beer law.[33] Assuming that the interfaces at the U1 locations in the unit cell are parallel to each other,[31] the maximum CdS shell thickness (L_{max}) equals reasonably to $l/2$ (Figure 2). Here, we define a parameter $f_1 = 2L/l$ ($0 \le f_1 \le 1$) to describe the percentage of the effective CdS exciton population in the CdS/ZnO-NA-U1 subdevice with a CdS shell thickness of L in respect to its maximal value in the unit cell. Actually, the f_1 means the percentage of the maximal contribution from effective CdS excitons in CdS/ZnO-NA-U1 subdevice has been realized by the formation of the CdS shell with a thickness of L. Extremely, $f_1 = 0$ means no CdS shell is formed on ZnO nanorods, and $f_1 = 1$ means the CdS exciton contribution to photocurrent generation reaches maximum as the interspacing between two ZnO nanorods has been completely filled by CdS subjected to the formation of two $l/2$-thick CdS shells on each of ZnO nanorods. Clearly, a larger f_1 in the range of $0 < f_1 < 1$ indicates an increased CdS exciton contribution to photocurrent generation as a result of increasing L.

On the other hand, the exciton diffusion length in MEH-PPV (L_D = 5−8 nm)[34,35] is rather short, and only the excitons generated within the L_D of the D/A interface are effective for photocurrent generation. Moreover, the interspacing l between the ZnO nanorods in our experiment is statistically averaged to be $l \approx 25$ nm,[18] in agreement with the previous reports by others.[36] Since $L_D \ll l/2$, there exists an ineffective region (Ex^{in}) in the polymer phase between two adjacent ZnO nanorods in MEH-PPV/ZnO-NA devices, and the excitons in the Ex^{in} region are actually ineffective for charge generation because they cannot reach the MEH-PPV/ZnO interface for dissociation within their lifetimes. Due to the presence of the Ex^{in} region, the increase in L within a certain range will not influence the polymer contribution by only reducing the ineffective polymer amount until the L reaches an optimal CdS shell thickness (L_{opt}) (inset to Figure 3).[18] In order to translate the ineffective polymer phase model into a mathematical expression in the present IMPS model, we introduce a factor f_2 ($0 \le f_2 \le 1$) to describe the percentage of the remaining effective exciton population in polymer phase after formation of CdS shell in the MEH-PPV/CdS-ZnO-NA-U1 subdevice with respect to the maximal effective polymer exciton population in

dx.doi.org/10.1021/jp509369n | J. Phys. Chem. C 2014, 118, 28462−28473

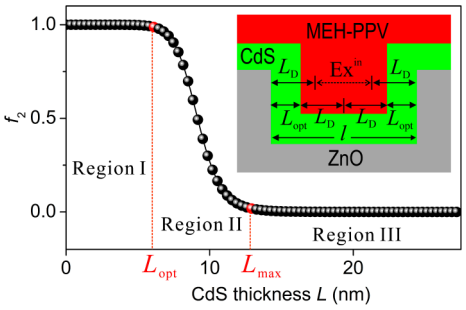

Figure 3. Typical f_2–L curve in the MEH-PPV/CdS-ZnO-NA-U1 subdevice with a given l for ZnO-NA and L_D for MEH-PPV. Inset illustrates the presence of Ex^{in} between ZnO nanorods with a interspacing of l nm and the absence of Ex^{in} between ZnO/CdS-core/shell nanorods at $L = L_{opt}$. Note, L_{opt} is the optimal CdS shell thickness above which the effective polymer exciton population starts to decrease, and L_{max} is the maximal CdS shell thickness at which the polymer excitons are absent.

the interspacing between two ZnO nanorods (i.e., $L = 0$; Figures S4 and S5 in Supporting Information),

$$f_2 = \left\{1/\left[1 - \left(-\frac{A}{g}\cdot\frac{(L+L_D)^2}{\varepsilon l + 2(L+L_D)}e^{-\varepsilon l/(L+L_D)} + \frac{A}{g}\cdot\frac{L_D^2}{\varepsilon l + 2L_D}e^{-\varepsilon l/(L_D)}\right)\right]\right\} \quad (1)$$

where A (s^{-1}) is a frequency constant, g (nm/s) is the CdS shell growth rate, ε (no dimension) is a constant depending on the intrinsic property of the polymer. Note, the parameter g is introduced in order to change the variable influencing f_2 from time t into CdS thickness L (Supporting Information). Therefore, f_2 correlates tightly with the nanoarray structure (l, L) and the intrinsic polymer properties (ε, L_D) in the MEH-PPV/CdS-ZnO-NA-U1 subdevice. Clearly, f_2 is merely L-dependent as the polymer and the original interspacing l in ZnO-NA are specified. The typical f_2–L curve takes a "Z" contour shown in Figure 3. The curve displays three characteristic regions. In region I, $f_2 = 1$ exists until increasing L up to L_{opt}, showing that the increased CdS shell thickness in the range of $L \le L_{opt}$ does not influence the population of effective excitons generated by polymer absorption. In region II, f_2 dramatically drops down to zero with further increasing L up to the maximal CdS shell thickness (L_{max}) when there is no polymer phase between ZnO/CdS-core/shell nanorods. The region III theoretically means that f_2 always equals to 0 for $L > L_{max} = l/2$, which will not be the case in practical devices. Obviously, f_2 is a parameter to describe the change in the effective exciton population in the polymer phase after formation of CdS shell in the MEH-PPV/CdS-ZnO-NA-U1 subdevice.

The f_2–L curve clearly shows that the effective excitons generated in polymer will decrease significantly for $L > L_{opt}$. Our calculations showed that, when the original nanoarray geometry (i.e., l) and the polymer excitonic property (i.e., L_D) are specified, the value of L_{opt} depends dominantly on A and ε, but almost not on g (Figure S6 in Supporting Information). On the basis of the L_D in MEH-PPV and the averaged l in ZnO-NA, our previous results demonstrated $L_{opt} \approx 6$ nm in MEH-PPV/ZC-NA solar cells.[18] Moreover, the typical time of growing the CdS shell with $L = 6$ nm needs about 4200 s during SILAR process (calculated from the summed times for adsorbing Cd^{2+} and S^{2-} ions multiplied by SILAR cycle numbers), thus the value of parameter g is estimated to be 1/700 nm/s. With the experimental value of $L_{opt} = 6$ nm as a reference, in combination with $g = 1/700$ nm/s, the parameters $A = 9 \times 10^9$ s^{-1} and $\varepsilon = 17.5$, and $L_{max} \approx 12.5$ nm as well, are obtained for the MEH-PPV/CdS-ZnO-NA-U1 subdevices (Figure S7 in Supporting Information). These values of parameter A, ε, and g are used for the calculations in the present IMPS model.

Additional assumptions are made as reported previously,[31] that is, (1) excitons are only generated in the D phase and dissociate at the D/A interface,[37,38] (2) photocurrent from the hole contribution is ignored,[39] (3) trapping (k_1) and detrapping (k_2) processes (Figure 1b) occur when the electrons transporting in the ZnO core,[40,41] (4) electric field effect is not considered,[30,42,43] (5) the exciton dissociation at the CdS/ZnO and MEH-PPV/CdS interfaces proceeds at the average rate of S_0 and S, respectively.[29]

3.1. Photocurrent $\Delta j_{11}(\omega)$ for CdS/ZnO-NA-U1 Subdevice. In the CdS/ZnO-NA-U1 subdevice, we define the effective exciton transport in the x direction normal to CdS/ZnO-U1 interface and the electron transport direction along y axis (Figure 4). Therefore, the excitons are generated in the

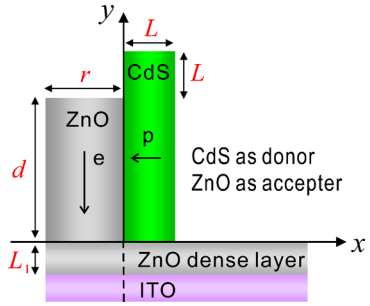

Figure 4. 2-D coordinate system for CdS/ZnO-NA-U1 subdevice. The position of CdS/ZnO-U1 interface is $x = 0$. The arrows represent the effective diffusion for excitons (p) in CdS and electrons (e) in ZnO nanorod under the illumination from ITO side.

CdS phase within the region of $0 \le x \le L$ and $0 \le y \le (d + L)$. Note, the excitons generated in the region of $0 \le x \le L$ and $d \le y \le (d + L)$ are regarded as additional ones to those in the region of $0 \le x \le L$ and $0 \le y \le d$; they diffuse vertically to the later region, then diffuse laterally toward the CdS/ZnO-U1 interface, and their contribution can be considered directly as a part of the excitons generated within $0 \le x \le L$ and $0 \le y \le d$.

3.1.1. Exciton Generation. During the IMPS measurements, the modulation illumination function imposed on a device is expressed as

$$I(x, y, t) = I_0 + I_0\delta e^{i\omega t} \quad (2)$$

where I_0 is the steady-state background light intensity (i.e., photon flux per m^2) and δ is the modulation depth. The continuity equation for the exciton density $p(x,y,t)$ at the position (x,y) in the region of $0 \le x \le L$ and $0 \le y \le (d + L)$ (Figure 4) under modulation illumination $I(x,y,t)$ from ITO side is written as[31]

dx.doi.org/10.1021/jp509369n | J. Phys. Chem. C 2014, 118, 28462–28473

$$\frac{\partial p(x, y, t)}{\partial t} = I(x, y, t)\alpha_0\theta e^{-\alpha_0 y} + D_{p0}\frac{\partial^2 p(x, y, t)}{\partial x^2} - \frac{p(x, y, t)}{\tau_{p0}} \quad (3)$$

where α_0 is the absorption coefficient of CdS, θ is the quantum efficiency of exciton generation upon photon absorption, D_{p0} and τ_{p0} are, respectively, the diffusion coefficient and lifetime of excitons in CdS. The exciton density under the modulated illumination can be written in the form of

$$p(x, y, t) = p_0(x, y) + \Delta p(x, y)e^{i\omega t} \quad (4)$$

where $p_0(x,y)$ is the steady-state exciton density and $\Delta p(x,y)e^{i\omega t}$ stands for the *ac* component of exciton density. Substituting eqs 2 and 4 into eq 3, then

$$\frac{\partial^2 \Delta p(x, y)}{\partial x^2} = \gamma_0^2 \Delta p(x, y) - \frac{I_0\delta\alpha_0 e^{-\alpha_0 y}\theta}{D_{p0}} \quad (5)$$

with

$$\gamma_0 = \sqrt{\frac{i\omega}{D_{p0}} + \frac{1}{D_{p0}\tau_{p0}}} \quad (6)$$

Two boundary conditions for eq 5 are given as

$$D_{p0}\frac{\partial \Delta p(x, y)}{\partial x}\bigg|_{x=0} = S_0 \Delta p(0, y) \quad (7)$$

$$\frac{\partial \Delta p(x, y)}{\partial x}\bigg|_{x=L} = 0 \quad (8)$$

where S_0 (cm/s) is the exciton dissociation rate at CdS/ZnO-U1 interface, and $S_0\Delta p(0,y)$ is the annihilation flux density of excitons at the CdS/ZnO-U1 interface. With the two boundary conditions, the *ac* component of exciton density $\Delta p(x,y)$ is obtained from eq 5 in the form of

$$\Delta p(x, y) = A_0 e^{\gamma_0 x} + B_0 e^{-\gamma_0 x} + C_0 e^{-\alpha_0 y} \quad (9)$$

with

$$A_0 = B_0 e^{-2\gamma_0 L} \quad (10)$$

$$B_0 = B_0^{/} e^{-\alpha_0 y} \quad (11)$$

$$C_0 = \frac{I_0\delta\alpha_0\theta}{\gamma_0^2 D_{p0}} \quad (12)$$

$$B_0^{/} = \frac{S_0 C_0}{D_{p0}\left[\left(\gamma_0 - \left(S_0/D_{p0}\right)\right)e^{-2\gamma_0 L} - \left(\gamma_0 + \left(S_0/D_{p0}\right)\right)\right]} \quad (13)$$

Considering that the effective CdS exciton generation has a percentage of $f_1 = 2L/l$ in the unit cell, the *ac* component of effective exciton density $[\Delta p^{/}(x,y,t)]$ generated in CdS shell in the CdS/ZnO-NA-U1 subdevice is expressed as

$$\Delta p^{/}(x, y, t) = \Delta p^{/}(x, y)e^{i\omega t} = \Delta p(x, y) f_1 e^{i\omega t} \quad (14)$$

3.1.2. Electron Generation. Since the exciton diffusion coefficient in CdS is rather high ($D_{p0} \sim 10^2$ cm^2/s),[32] it takes about 10^{-14} s for the excitons in CdS to diffuse across the CdS shell with L = 10 nm according to the relationship $t = L^2/D_{p0}$. Therefore, the time delay between exciton generation and electron generation can be ignored in CdS/ZnO-NA-U1 subdevice, similar to the case in DSCs.[26] Given that the excitons generated at the position (x,y) in CdS phase dissociate at position $(0,y)$ $(0 \le y \le d)$ with the ratio of injected electrons to dissociated excitons is 100%, the electron density $n^{/}(x,y,t)$ in ZnO nanorod is described as[31]

$$n^{/}(x, y, t) = n^{/}(0, y, t) = D_{p0}\frac{\partial^2 \Delta p^{/}(x, y, t)}{\partial x^2}\bigg|_{x=0} \quad (15)$$

Substituting eqs 9−14 into eq 15, then

$$n^{/}(x, y, t) = D_{p0} B_0^{/} f_1 \gamma_0^2 (e^{-2\gamma_0 L} + 1)e^{-\alpha_0 y}e^{i\omega t} \quad (16)$$

3.1.3. Electron Transport and Collection. To reach ITO substrate for photocurrent generation, the electrons injected into ZnO need to diffuse through ZnO nanorod $(0 \le y \le d)$ and ZnO dense layer $(-L_1 \le y \le 0$; Figure 4). Moreover, we use the electron injection rate (v_{th}) to describe the electron injection from ZnO nanorod to ZnO dense layer at the nanorod/dense layer interface $(y = 0)$ and use a constant rate k_{ext} to describe the electron extraction from the ZnO dense layer into ITO substrate. With the electron density $n^{/}(x,y,t)$ generated by CdS absorption, the *ac* component of the photocurrent $\Delta j_{11}(\omega)$ in CdS/ZnO-NA-U1 subdevice can be obtained by solving equations for the electron transport and collection processes as described in polymer/ZnO-NA devices.[31] In order to provide a complete description of the electron transport and collection dynamics in the CdS/ZnO-NA-U1 subdevice that is actually a novel inorganic case, here we provide the continuity equations and related solutions for these processes in details.

In ZnO nanorod $(0 \le y \le d)$, the excess electron densities in the conduction band (i.e., $n(x,y,t)$) and in the trap states (i.e., $N(x,y,t)$) are described as[31]

$$\frac{\partial n(x, y, t)}{\partial t} = n^{/}(x, y, t) + D_e\frac{\partial^2 n(x, y, t)}{\partial y^2} - k_1 n(x, y, t) + k_2 N(x, y, t) - \frac{n(x, y, t) - n_0}{\tau_e} \quad (17)$$

$$\frac{\partial N(x, y, t)}{\partial t} = k_1 n(x, y, t) - k_2 N(x, y, t) \quad (18)$$

where $D_e = D_{cb}k_2/k_1$ is the effective diffusion coefficient of electrons with D_{cb} being the diffusion coefficient of electrons in conduction band, k_1 and k_2 are the first-order rate constants for trapping and detrapping, τ_e is the electron lifetime in conduction band, and n_0 is the equilibrium electron density in the dark. The excess electron density $n(x,y,t)$ in the conduction band of ZnO nanorod under the modulated illumination can be separated into a steady-state density $n_0(x,y)$ and an *ac* component $\Delta n(x,y)e^{i\omega t}$,

$$n(x, y, t) = n_0(x, y) + \Delta n(x, y)e^{i\omega t} \quad (19)$$

and the same to $n(x,y,t)$, the $N(x,y,t)$ can be written as

$$N(x, y, t) = N_0(x, y) + \Delta N(x, y)e^{i\omega t} \quad (20)$$

where $N_0(x,y)$ is the steady-state density and $\Delta N(x,y)e^{i\omega t}$ is the *ac* component density. Based on eqs 15−20, the continuity equation for the excess electron density $\Delta n(x,y)$ in the conduction band of ZnO nanorod is expressed as

dx.doi.org/10.1021/jp509369n | J. Phys. Chem. C 2014, 118, 28462−28473

$$\frac{\partial^2 \Delta n(x,y)}{\partial y^2} = \beta^2 \Delta n(x,y) - \frac{D_{p0}}{D_e} B_0' f_1 \gamma_0^2 (e^{-2\gamma_0 L} + 1) e^{-\alpha_0 y} \tag{21}$$

with

$$\beta = \sqrt{\frac{-\omega^2 + i\omega(k_1 + k_2)}{D_e(i\omega + k_2)} + \frac{1}{D_e \tau_e}} \tag{22}$$

For the electrons with a density of $\Delta n(x,y)$ transport along y direction toward the dense layer, two boundary conditions are given as

$$\left.\frac{\partial \Delta n(x,y)}{\partial y}\right|_{y=d} = 0 \tag{23}$$

$$\left. D_e \frac{\partial \Delta n(x,y)}{\partial y}\right|_{y=0} = v_{th} \Delta n(x,0) \tag{24}$$

where v_{th} is the injection rate (cm/s) of electrons from the ZnO nanorod into the dense layer at position $(x,0)$ $(-r \le x \le 0)$. Accordingly, with the above boundary conditions, the solution of eq 21 takes the form

$$\Delta n(x,y) = A_1 e^{\beta y} + B_1 e^{-\beta y} + C_1 e^{-\alpha_0 y} \tag{25}$$

with

$$A_1 = \frac{B_1 \beta e^{-\beta d} + C_1 \alpha_0 e^{-\alpha_0 d}}{\beta e^{\beta d}} \tag{26}$$

$$B_1 = \frac{\left(\beta - \frac{v_{th}}{D_e}\right)\alpha_0 e^{-\alpha_0 d} - \left(\alpha_0 + \frac{v_{th}}{D_e}\right)\beta e^{\beta d}}{\left(\beta + \frac{v_{th}}{D_e}\right)\beta e^{\beta d} - \left(\beta - \frac{v_{th}}{D_e}\right)\beta e^{-\beta d}} C_1 \tag{27}$$

$$C_1 = \frac{D_{p0}\gamma_0^2 (e^{-2\gamma_0 L} + 1)}{D_e(\beta^2 - \alpha_0^2)} B_0' f_1 \tag{28}$$

In the region $-L_1 \le y \le 0$, the exciton generation in CdS is no longer existing to affect the transport dynamics, and the excess electron density $[n_1(x,y,t)]$ in the ZnO dense layer is injected from the ZnO nanorod at an electron injection rate of v_{th} (cm/s; Figure 4), the continuity equation for the electron density $n_1(x,y,t)$ and the electron density $[N_1(x,y,t)]$ in the trap states of ZnO in the dense layer are expressed as

$$\frac{\partial n_1(x,y,t)}{\partial t} = D_e \frac{\partial^2 n_1(x,y,t)}{\partial y^2} - k_1 n_1(x,y,t) + k_2 N_1(x,y,t) - \frac{n_1(x,y,t)}{\tau_e} \tag{29}$$

$$\frac{\partial N_1(x,y,t)}{\partial t} = k_1 n_1(x,y,t) - k_2 N_1(x,y,t) \tag{30}$$

With a transform of electron density of $n_1(x,y,t)$ and $N_1(x,y,t)$ into steady-state and *ac* components, we obtain,

$$n_1(x,y,t) = n_{10}(x,y) + \Delta n_1(x,y) e^{i\omega t} \tag{31}$$

$$N_1(x,y,t) = N_{10}(x,y) + \Delta N_1(x,y) e^{i\omega t} \tag{32}$$

where both $n_{10}(x,y)$ and $N_{10}(x,y)$ are the steady-state densities, and both $\Delta n_1(x,y)e^{i\omega t}$ and $\Delta N_1(x,y)e^{i\omega t}$ are the *ac* component densities. Based on eqs 29−32, the continuity equation for the excess electron density $\Delta n_1(x,y)$ in the conduction band of ZnO dense layer is expressed as

$$\frac{\partial^2 \Delta n_1(x,y)}{\partial y^2} = \beta^2 \Delta n_1(x,y) \tag{33}$$

As the electron density at the nanorod/dense layer interface $(y = 0)$ is determined by the electron injection rate v_{th}, and the electrons in the ZnO dense layer are extracted into ITO substrate at the dense layer/ITO interface $(y = -L_1)$ with a constant rate k_{ext}, the boundary conditions are obtained as

$$\left. D_e \frac{\partial \Delta n_1(x,y)}{\partial y}\right|_{y=0} = v_{th} \Delta n(x,0) \tag{34}$$

$$\left. D_e \frac{\partial \Delta n_1(x,y)}{\partial y}\right|_{y=-L_1} = k_{ext} \Delta n_1(x,-L_1) \tag{35}$$

Accordingly, the solution of eq 33 is

$$\Delta n_1(x,y) = A_2 e^{\beta y} + B_2 e^{-\beta y} \tag{36}$$

with

$$A_2 = \frac{v_{th}}{\beta D_e}(A_1 + B_1 + C_1) + B_2 \tag{37}$$

$$B_2 = \frac{v_{th}}{\beta D_e} \times \frac{(A_1 + B_1 + C_1)[\beta - (k_{ext}/D_e)]e^{-\beta L_1}}{[\beta + (k_{ext}/D_e)]e^{\beta L_1} - [\beta - (k_{ext}/D_e)]e^{-\beta L_1}} \tag{38}$$

With a large enough k_{ext} value for the electron extraction, the solution for the diffusion-limited short circuit can be obtained from eq 36, and the *ac* component of the photocurrent in CdS/ZnO-NA-U1 subdevice is given by

$$\Delta j_{11}(\omega) = qD_e \left.\frac{\partial \Delta n_1(x,y)}{\partial y}\right|_{y=-L_1} = q\beta D_e (A_2 e^{-\beta L_1} - B_2 e^{\beta L_1}) \tag{39}$$

3.2. Photocurrent $\Delta j_{12}(\omega)$ for MEH-PPV/CdS-ZnO-NA-U1 Subdevice. In the MEH-PPV/CdS-ZnO-NA-U1 subdevice, we define the effective exciton transport along the x direction normal to MEH-PPV/CdS-U1 interface and the electron transport direction along y axis (Figure 5). Therefore, the excitons are generated in the MEH-PPV within the region of $0 \le x \le l - 2L$ and $L \le y \le d + L + L_2$. Note, the excitons

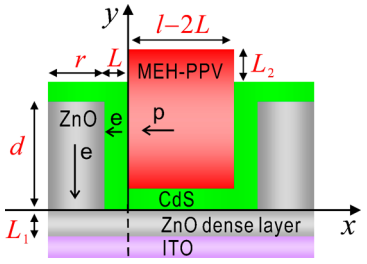

Figure 5. 2-D coordinate system for MEH-PPV/CdS-ZnO-NA-U1 subdevice with MEH-PPV as donor and ZnO/CdS-core/shell nanorod as acceptor. The arrows represent the effective diffusion for excitons (p) in MEH-PPV and electrons (e) in CdS shell and ZnO nanorod under the illumination from ITO side.

dx.doi.org/10.1021/jp509369n | J. Phys. Chem. C 2014, 118, 28462−28473

generated in the region of $0 \le x \le l - 2L$ and $d + L \le y \le d + L + L_2$ are regarded as additional ones to those in the region of $0 \le x \le l - 2L$ and $L \le y \le d + L$; they diffuse vertically to the later region followed by a diffusion laterally toward the MEH-PPV/CdS-U1 interface, and their contribution can be considered directly as a part of the excitons generated within $0 \le x \le l - 2L$ and $L \le y \le d + L$.

3.2.1. Exciton Generation. The continuity equation for the exciton density $p_p(x,y,t)$ at the position (x,y) in the MEH-PPV phase under the illumination from the ITO side is expressed as[31]

$$\frac{\partial p_p(x,y,t)}{\partial t} = I(x,y,t)\alpha_p\theta e^{-\alpha_p y} + D_p\frac{\partial^2 p_p(x,y,t)}{\partial x^2} - \frac{p_p(x,y,t)}{\tau_p} \quad (40)$$

where α_p is the absorption coefficient of MEH-PPV, D_p and τ_p are the diffusion coefficient and lifetime of excitons in MEH-PPV. Assuming that the polymer excitons dissociate at the polymer/CdS interface with a rate of S (cm/s), the *ac* component of exciton density $\Delta p_p(x,y)$ can be obtained by solving eq 40 under appropriate boundary conditions (Supporting Information). In order to get a comprehensive evaluation of the CdS shell thickness on the population of effective excitons in polymer, the f_2 factor is considered for the effective exciton density $p_p(x,y,t)$ in the polymer phase, and the *ac* component of effective exciton density $[\Delta p_p'(x,y,t)]$ in the MEH-PPV/CdS-ZnO-NA-U1 subdevice is expressed as

$$\Delta p_p'(x,y,t) = \Delta p_p'(x,y)e^{i\omega t} = \Delta p_p(x,y)f_2 e^{i\omega t} \quad (41)$$

3.2.2. Electron Generation, Transport, and Collection. Different from the CdS/ZnO-NA-U1 subdevice, the time delay between exciton generation and electron generation cannot be ignored in the MEH-PPV/CdS-ZnO-NA-U1 subdevice due to the quite low exciton diffusion coefficient ($D_p \sim 10^{-3}$ cm^2/s)[44] in the polymer phase, and it will manifest itself as a phase shift in a form of $\phi_n(\omega) = \pi(\omega/\omega_0)^N$, where ω_0 (rad/s) is a constant correlating with the exciton diffusion property of polymer and the configuration of devices, and N is the ideality factor correlating with the device structure.[31] On the other hand, since the time for electrons to diffuse across the CdS shell with a thickness of 10 nm is approximately within 10 ns[18] and the electron injection from CdS into ZnO normally occurs on a time scale from picoseconds up to nanoseconds.[45,46] It is reasonable to ignore the transit time for the electrons generated by the polymer absorption to diffuse across the CdS shell toward ZnO core nanorod in the MEH-PPV/CdS-ZnO-NA-U1 subdevice; moreover, ZnO/CdS-core/shell nanorod can be simply regarded as the ZnO nanorod for electron transport with a radius increased up to $r + L$ nm. Therefore, after obtaining the effective exciton density (eq 41), the transport and collection dynamics of the electrons injected into ZnO nanorod for photocurrent generation in MEH-PPV/CdS-ZnO-NA-U1 subdevice are the same to that in polymer/ZnO-NA solar cells described previously.[31] With the exciton density $\Delta p_p'(x,y,t)$, the *ac* component of the photocurrent $\Delta j_{12}(\omega)$ in MEH-PPV/CdS-ZnO-NA-U1 subdevice is obtained by solving equations for the generation, transport, and collection processes of photogenerated electrons, as described in polymer/ZnO-NA devices (Supporting Information).

3.3. Photocurrent $\Delta J(\omega)$ Generated by Unit Cell. The *ac* photocurrent density $\Delta J_1(\omega)$ generated by the interfaces at the U1 location is the combined contribution from CdS/ZnO-NA-U1 and MEH-PPV/CdS-ZnO-NA-U1 subdevices, that is, $\Delta J_1(\omega) = 2\Delta j_{11}(\omega) + \Delta j_{12}(\omega)$. The total *ac* photocurrent density $\Delta J(\omega)$ generated by a unit cell is the weighted average of photocurrent densities generated by the subdevices defined by the interfaces at the U1, U2, and U3 locations according to the ITO areas occupied by them, even though the $\Delta J_2(\omega)$ and $\Delta J_3(\omega)$ generated by the subdevices at the U2 and U3 locations are defined to be zero (Figure S3). The *ac* photocurrent conversion efficiency $\varphi(\omega)$ is given by $\varphi(\omega) = \Delta J(\omega)/(I_0\delta\theta q)$. Considering the *RC* attenuation effect $F(\omega) = (1 + i\omega RC)^{-1}$ of the electrode on experimental IMPS responses,[26,29,47] the measured IMPS response $\Phi_m(\omega)$ is expressed as

$$\Phi_m(\omega) = \frac{\Delta J(\omega)}{I_0\delta\theta q}\cdot\frac{1}{1 + i\omega RC} \quad (42)$$

where R and C are the resistance and capacitance of collection electrode, respectively.

3.4. Theoretical Expectations. The dependences of IMPS responses on CdS shell thickness L calculated from eq 42 are shown in Figure 6. All of the calculated IMPS responses appear

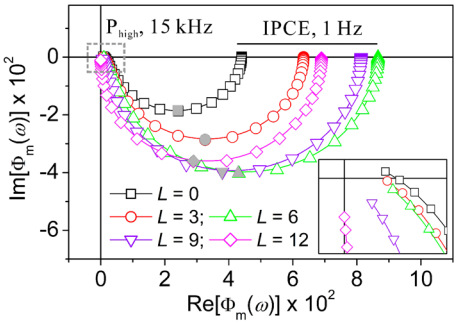

Figure 6. Calculated IMPS responses upon different L values with calculating frequency from 1 Hz to 15 kHz. The parameters for calculation are $\omega_0 = 2.37 \times 10^5$ rad/s, $N = 0.6$, $S = 400$ cm/s, $C = 23$ μF, $D_e = 5 \times 10^{-4}$ cm^2/s, $k_1 = 5 \times 10^5$ s^{-1}, $k_2 = 5 \times 10^3$ s^{-1}, and $\tau_e = 2$ ms. Moreover, $S_0 = 0$ for $L = 0$ nm, $S_0 = 1500$ for $L \neq 0$ nm. The inset magnifies the IMPS spectra around P_{high} points; the solid symbols on the plots identify the f_{min} (=320 Hz) points.

in the fourth quadrant (positive real, negative imaginary) of the complex plane, similar to the MEH-PPV/ZnO-NA devices.[31] For all the calculations in this paper, $\theta = 1$, $\delta = 0.1$, $v_{th} = 10^4$ cm/s, $k_{ext} = 10^6$ cm/s, $R = 20$ Ω, $L_1 = 40$ nm, and $q = 1.6 \times 10^{-19}$ C are given by referring to the previous report,[31] and the experimental $d = 400$ nm, $r = 14$ nm, and $l = 25$ nm are obtained from the ZnO-NA for preparing the ZC-NA structure;[18] moreover, $D_p = 1.1 \times 10^{-3}$ cm^2/s and $\tau_p = 455 \times 10^{-12}$ s,[34] and $\alpha_p = 10^5$ cm^{-1} for MEH-PPV,[48] while $D_{p0} = 0.41 \times 10^3$ cm^2/s and $\tau_{p0} = 3.2 \times 10^{-3}$ s,[32] and $\alpha_0 = 10^4$ cm^{-1} for CdS[49] were adopted from literature.

The crossing point of the IMPS responses with the positive real axis at low frequency is referred to as IPCE point which provides a direct estimation of the incident photon-to-current conversion efficiency (IPCE) as the photocurrent is divided by photon flux, and that at high frequency to as the P_{high} point that gives an evaluation of the exciton diffusion effect (i.e., $\phi_n(\omega)$) on the electron transport.[29,31] The calculated IPCE first increases with increasing L up to 6 nm; however, further

dx.doi.org/10.1021/jp509369n | J. Phys. Chem. C 2014, 118, 28462−28473

increase in L up to >6 nm results in a decreased rather than increased IPCE, suggesting the presence of L_{opt} = 6 nm for MEH-PPV/ZC-NA devices. At the first glance, the P_{high} point location does not change remarkably with increasing L, but a magnified view (inset to Figure 6) shows that the P_{high} point location actually moves toward the origin as L increases, inferring a decreased phase shift $\phi_n(\omega)$ effect on electron transport dynamics.[31] The decreased phase shift $\phi_n(\omega)$ effect with increasing L can be understood by the fact that the increased CdS layer reduces the diffusion time (or distance) of the excitons in polymer phase.

Figure 7a shows the dependences of calculated IMPS responses on S and S_0. Increasing the exciton dissociation rate S at the MEH-PPV/CdS-U1 interface leads to a slightly enhanced phase shift $\phi_n(\omega)$ effect with the P_{high} point biasing away from the origin and a larger IPCE, which is similar to the findings in MEH-PPV/ZnO-NA devices.[31] Different from the S, however, the exciton dissociation rate S_0 at the CdS/ZnO-U1 interface does not evidently affect the shape of IMPS responses (Figure 7b), indicating that S_0 can be assigned an arbitrary value during calculation. Further calculations showed that the IMPS responses are also independent of S_0, even when assuming the absorption coefficient of shell layer is as high as $\alpha_0 \geq 10^5$ cm^{-1}, for example (Figure S8 in Supporting Information), only with a remarkably increased IPCE for the increased α_0 from 10^4 to 10^5 cm^{-1}. The unchanged shape of the IMPS responses upon changing S_0 suggests that the electron transport dynamics and the photocurrent generation in the MEH-PPV/ZC-NA solar cells are not affected by the exciton dissociation at the CdS/ZnO-U1 interface, for which the reason is probably due to the good exciton diffusion property in the shell layer. The calculated dependences of IMPS responses on S and S_0 demonstrate that the IPCE of MEH-PPV/ZC-NA solar cells are dominantly relevant to the polymer exciton dissociation but not affected by the CdS exciton dissociation.

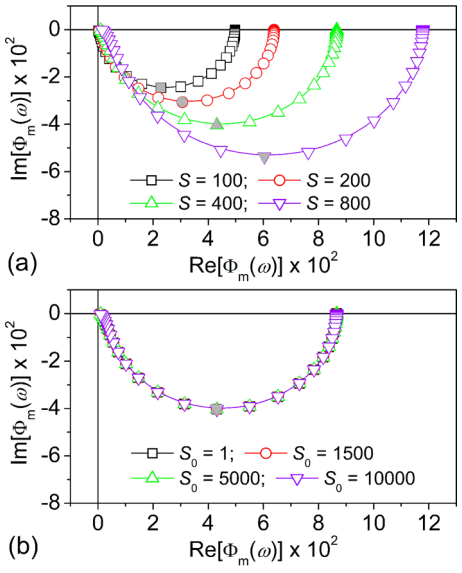

Figure 7. Calculated IMPS responses upon different S (a) and S_0 (b) values with calculating frequency from 1 Hz to 15 kHz. The parameters for calculation are L = 6 nm, $\omega_0 = 2.37 \times 10^5$ rad/s, N = 0.6, C = 23 μF, $D_e = 5 \times 10^{-4}$ cm^2/s, $k_1 = 5 \times 10^5$ s^{-1}, $k_2 = 5 \times 10^3$ s^{-1}, and τ_e = 2 ms. S_0 = 1500 cm/s and S = 400 cm/s are used for calculations in (a) and (b), respectively. The solid symbols on the plots identify the f_{min} (=320 Hz) points.

4. RESULTS AND DISCUSSION

4.1. Comparison between Calculated and Experimental Results. The MEH-PPV/ZC-NA devices with L = 0−8 nm were fabricated for experiments. The steady-state J−V characteristics (Figure S9 and Table S1 in Supporting Information) under monochromatic illumination (15.85 mW/cm^2) showed that the device J_{sc} first increases with increasing L up to 6 nm, then decreases by further increasing L up to 8 nm, while the V_{oc} increases from 0.348 to 0.766 V with the increase in L from 0 to 6 nm and further increase in L only leads to a slight increase in V_{oc}. The J−V results under the monochromatic illumination are identical to that obtained under AM 1.5 illumination (100 mW/cm^2).[18] The dynamic IMPS responses of these solar cells are shown in Figure 8. Clearly, the measured IMPS responses appear in the forth quadrant of the complex plane, the IPCE initially increases within L = 0−6 nm but decreases with further increasing L to 8 nm, and the P_{high} points approach the origin with increasing L (inset to Figure 8); all of the changes in the shape of experimental IMPS responses confirms well the model expectations (Figure 6). The good accordance between the experimental and calculated IMPS results suggests that our model has captured the main characteristics of photovoltaic process in polymer/ZC-NA devices and can provide mechanistic understandings of the charge transport dynamics and device performance under the formation of core/shell-structured electron transport channels.

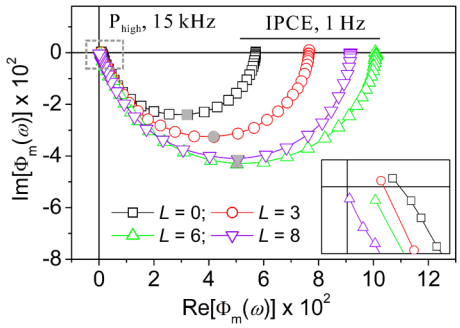

Figure 8. Measured IMPS responses of the MEH-PPV/ZC-NA devices with different L values. The inset magnifies the IMPS spectra around P_{high} points; the solid symbols on the plots identify the f_{min} points.

4.2. CdS Shell Effects on Photocurrent Generation. The IPCE values of the solar cells can be directly obtained from the IMPS responses. As shown in Figure 9, the IPCE values obtained from the dynamic IMPS measurements are close to that obtained from the steady-state J−V measurements (Figure S9 and Table S1) under monochromatic illumination. Moreover, the L-dependence of IPCE data from the IMPS and J−V measurements agrees with those from the IPCE curves at 470 nm (Figure S10 in Supporting Information). Figure 9 also compares the correlations between the L-dependences of the experimental IPCE data and the calculated f_1 or f_2 values (refer to Table 1). Increasing L from 0 to 8 nm leads to an always increase in the CdS contribution (i.e., f_1), but an unchanged MEH-PPV contribution (i.e., f_2) within $L \leq 6$ nm followed by a significantly decreased f_2 with further increasing L up to 8 nm. Clearly, the increase in IPCE, and J_{sc} (Figure S9 and Table S1)

dx.doi.org/10.1021/jp509369n | J. Phys. Chem. C 2014, 118, 28462−28473

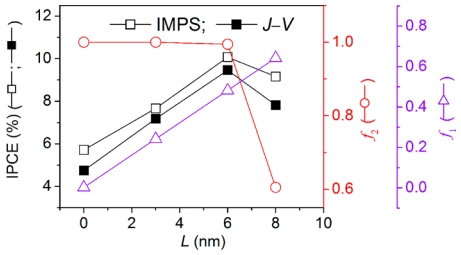

Figure 9. *L*-Dependences of the experimental IPCE data from IMPS and *J*–*V* measurements and the calculated f_1 and f_2 values from the model.

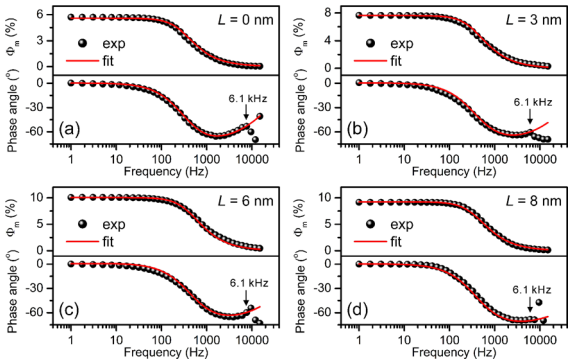

Figure 10. Measured and fitted IMPS responses in the form of Bode plots for the devices with *L* = 0 (a), 3 (b), 6 (c), and 8 nm (d). The arrows on the plots identify the datum points of 6.1 kHz.

as well, within the range of $L \leq 6$ nm is mainly due to the increased absorption contribution to photocurrent generation from the CdS shell that imposes no influence on MEH-PPV contribution, but the decreased IPCE (J_{sc}) for further increasing *L* up to 8 nm is due to the remarkably reduced MEH-PPV absorption contribution to photocurrent generation. These results quantitatively demonstrate that polymer is the dominant absorption material in the MEH-PPV/ZC-NA solar cells, in agreement with our previous conclusion.[18]

4.3. Fitting IMPS Responses. The mean transit time (τ_D) for the electron transport through the ZnO nanorod to collection electrode was calculated from the frequency f_{min} of the lowest imaginary component of experimental IMPS response by the relation $\tau_D = 1/(2\pi f_{min})$. The transit time τ_D is given in Table 1. To get a deep insight into the charge generation and transport dynamics, the experimental IMPS responses are fitted to the model (eq 42). Because the phase plot can provide a sensitive diagnostic analysis of the electron transit time τ_D, electron diffusion coefficient D_e, and $\phi_n(\omega)$ effect,[26,29] the best method to fit an experimental IMPS response is to use its corresponding Bode plots rather than its complex plane form. The fitting processes were done by three steps as described previously.[31] First, the *S* is directly evaluated from the IPCE points of the measured IMPS responses according to eq 42. Second, the ω_0 (10^6 rad/s) for the MEH-PPV/ZnO-NA device[31] is applied as a temporary value to the MEH-PPV/ZC-NA devices, and the order of magnitude is taken to be 10^5 s^{-1} for k_1, with $k_1 > k_2$,[50] the D_e value is obtained with $N = 1$ after inserting other parameters (α_0, α_p, D_{p0}, D_p, τ_{p0}, τ_p, ν_{th}, k_{ext}, τ_e, *l*, *d*, *r*, L_1, *q*, I_0, δ, θ) into eq 42, and simultaneously varying D_e, *R*, and *C* until a good accordance with the experimental f_{min} value and the magnitude plot in the whole frequency range is obtained. At last, with changing *N* and ω_0 values simultaneously, the phase angle plot in the whole frequency range gets satisfactorily fitted. Figure 10 shows the fitted IMPS responses. Note that, as S_0 does not affect the IMPS response (Figure 7b), the S_0 for the MEH-PPV/ZC-NA devices was defined as 1500 cm/s according to the relation $S_0 \approx R_e S$, in which R_e is the ratio of the exciton binding energies between MEH-PPV (~600 meV[51]) and CdS (~180 meV[19]); moreover, the τ_e value in each device (Table 1) was measured with IMVS (Figure S11 in Supporting Information) and used for fitting. Also, noticeably, the Bode plots clearly show that all the experimental IMPS responses are altered at 6.1 kHz, which is possibly due to the slow detrapping of electrons in comparison to the modulation frequency.[26,50] All of the fitted parameters are collected in Table 1.

4.3.1. CdS Shell Effects on Electron Transport. It has been demonstrated that the CdS shell may provide additional absorption to increase the charge generation but reduce the effective polymer excitons for charge generation, resulting in a charge generation strongly correlated with CdS shell thickness in the MEH-PPV/ZC-NA devices (Figure 9). The fitted *S* for the MEH-PPV/ZnO-NA (*L* = 0 nm) devices is almost the same to that for the MEH-PPV/ZC-NA (*L* = 3–8 nm) ones, which suggests that ZnO and CdS are similarly effective for dissociating the polymer excitons, in a good agreement with our previous PL results.[18]

During the electron transport to collection electrode, the surface defects on the ZnO nanorods will affect the transport dynamics by trapping (k_1) and detrapping (k_2) processes,[52,53] as depicted in Figure 1. Shown in Figure 11 are the *L*-

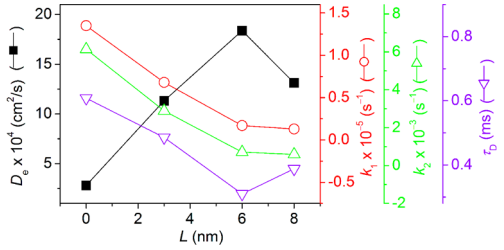

Figure 11. Dependences of D_e, k_1, k_2, and τ_D on CdS shell thickness *L*.

Table 1. Fitted Parameters for the MEH-PPV/ZC-NA Devices with Different *L* Values

L (nm)	f_1[a]	f_2[a]	τ_D[b] (ms)	τ_e[c] (ms)	ω_0 (rad/s)	*N*	*S* (cm/s)	D_e (cm^2/s)	k_1 (s^{-1})	k_2 (s^{-1})	*C* (μF)
0	0.00	1.00	0.61	0.76	2.21×10^6	0.425	550	2.81×10^{-4}	1.35×10^5	6.14×10^3	25.78
3	0.24	1.00	0.49	0.95	2.68×10^6	0.403	556	11.32×10^{-4}	0.68×10^5	2.89×10^3	21.31
6	0.48	0.99	0.31	1.87	3.41×10^6	0.360	557	18.37×10^{-4}	0.17×10^5	0.71×10^3	18.29
8	0.64	0.61	0.39	2.35	3.62×10^6	0.380	557	13.12×10^{-4}	0.13×10^5	0.59×10^3	20.61

[a]The values of parameter f_1 and f_2 are calculated from the structure of core/shell nanoarray and the intrinsic polymer property. [b]The electron transit time measured with IMPS. [c]The electron lifetime measured with IMVS.

dx.doi.org/10.1021/jp509369n | J. Phys. Chem. C 2014, 118, 28462–28473

dependences of D_e, k_1, k_2, and τ_D. Clearly, a smaller τ_D is accompanied by a larger D_e. The L-dependence of D_e is similar to that of IPCE (Figure 9), suggesting a strong correlation between the electron density in ZnO conduction band and D_e in the MEH-PPV/ZC-NA solar cells.[54−57] Moreover, both k_1 and k_2 decrease significantly with increasing L up to 6 nm, further increase in L hardly changes their values. As k_1 is the first-order rate constant for the surface states to trap electrons, the L-dependence of k_1 indicates that the passivation of ZnO surface defect gets to the largest extent at L = 6 nm, which is consistent with our previous PL results.[18] The k_2 is the first-order rate constant for detrapping, and the change trend of k_2 with increasing L is similar to that of k_1, indicating that a slower trapping rate is accompanied by a slower detrapping process. Note, the reduced surface defects on ZnO for trapping electrons, and the reduced charge recombination as well (Table 1) will allow more photogenerated electrons to accommodate in ZnO conduction band, also favoring the increases in the electron concentration therein and the photocurrent generation in device. For L = 0−8 nm, even though changed very slightly, the fitted N has opposite L-dependence to D_e and IPCE (Table 1), which agrees with the conclusion that the N value correlates with the concentration of the electrons that diffuse directly (i.e., DD transport) toward collection electrode.[31]

The crucial photovoltaic processes in the HPSCs involve the diffusion of photogenerated polymer excitons toward the D/A interface for dissociation into free charge carriers and the effective transport to collection electrodes of the charge carriers before recombination. The exciton diffusion in polymer phase has a phase shift $\phi_n(\omega)$ effect on electron transport.[29,31] Our previous calculations[31] show that S, N, and D_e can influence the $\phi_n(\omega)$ effect, among which either decreased N or an increased D_e will cause an enhanced $\phi_n(\omega)$ effect by making the P_{high} point biasing away from the origin. The experimental IMPS responses show that the P_{high} point moves toward the origin with increasing L, suggesting a reduced $\phi_n(\omega)$ effect (Figure 8). The comparable S for the devices with L = 0−8 nm suggests that the changed $\phi_n(\omega)$ effect is not originating from S. Moreover, with increasing L from 0 to 6 nm, we get the slightly decreased N and significantly increased D_e values (Table 1), which are actually accompanied by a reduced $\phi_n(\omega)$ effect (Figure 8), indicating thereby that N and D_e are also not the reason for the observed $\phi_n(\omega)$ effect. Fitted results show that ω_0 has a value of 2.21×10^6 rad/s for L = 0, in agreement with the value for MEH-PPV/ZnO-NA device.[31] With increasing L, the fitted ω_0 gets slightly increased (Table 1). According to $\phi_n(\omega) = \pi(\omega/\omega_0)^N$, an increased ω_0 will lead to a reduced $\phi_n(\omega)$ effect under the comparable N values. Intrinsically, ω_0 is a constant correlating with the exciton diffusion property of polymer. However, we have found that the ω_0 value (2.25×10^6 rad/s) for MEH-PPV/ZnO-NA bulk cells[31] is much higher than that for the MEH-PPV/TiO_2 bilayer devices (6×10^4 rad/s),[29] indicating that the exciton diffusion property in the polymer also tightly correlates with device architecture. In fact, the MEH-PPV/ZC-NA solar cells with L = 0−8 nm actually have a comparable ω_0 due to the similar aligned bulk architecture in them (Table 1). The reduced $\phi_n(\omega)$ with increasing L in the MEH-PPV/ZC-NA solar cells is eventually attributed to the decreased exciton diffusion time (or distance) of the excitons in the polymer phase as a result of the increased L, in agreement with the theoretical prediction (Figure 6). Moreover, in the IMPS model, the RC attenuation effect of electrode is considered, where the resistance R is normally determined by the sheet resistance of the ITO substrate (10−20 Ω)[26,47,58] and thereby is set to be a constant of 20 Ω in the IMPS fitting. Since RC represents the charging/discharging time of a device, a smaller RC will result in a smaller transit time τ_D,[31] which is confirmed by the L-dependence of the fitted capacitance values (Table 1).

4.3.2. Remarks. The IMPS model established in this paper captures the main characteristics of the photovoltaic processes in polymer/ZC-NA devices and provides new insights into the structure-related electron transport dynamics and device performance. Moreover, the IMPS model is expected to find extended applications to other oxide-based core/shell nanoarray with the shells having different complementary absorption properties, such as, the shells with a small band gap (e.g., $CuInS_2$, Sb_2S_3, CZTS) for absorbing photons, or the shells with a wide band gap (e.g., TiO_2, ZnO) by which the additional charge generation in the shells is eliminated. Furthermore, the polymer used in this model could be replaced by other excitonic absorption materials, no matter they are organics or inorganics, after a revised $\phi_n(\omega) = \pi(\omega/\omega_0)^N$ effect, depending on the exciton diffusion properties in the absorption materials.

5. CONCLUSION

In this paper, we have established an IMPS model for dynamic characterization of the HPSCs based on ZnO/CdS-core/shell nanorod by considering the main characteristics of photovoltaic processes, the effective shell absorption contribution (f_1) and the effective polymer absorption contribution (f_2). The main expectations of the model are satisfactorily confirmed by the experimental data of the MEH-PPV/ZC-NA devices. It is theoretically demonstrated that the charge generation due to the exciton dissociation at the D/A interfaces provided by nanorod side faces dominates the photocurrent generation in polymer/nanorod array solar cells. The calculations based on the IMPS model reveal that the IPCE (or J_{sc}) of MEH-PPV/ZC-NA solar cells depends dominantly on f_1, f_2, and the polymer exciton dissociation rate S at the MEH-PPV/CdS interfaces at the ZnO/CdS-core/shell nanorod side faces, but is independent of the CdS exciton dissociation rate S_0 at the CdS/ZnO interfaces therein; moreover, calculated results quantitatively demonstrate that the polymer is the dominant absorption material in the MEH-PPV/ZC-NA solar cells, in which the photocurrent generation is dominantly the competitive results of f_1 and f_2 contributions subjected to the change in L. Fitting the experimental IMPS data of MEH-PPV/ZC-NA solar cells into the model demonstrates that, the first-order rate constant k_1 for the surface states on ZnO nanorods to trap electrons remains nearly unchanged after the surface defects have been passivated to the largest extent. Moreover, the L-dependence of first-order rate constant k_2 for detrapping electrons is similar to that of k_1, which indicates that a slower trapping rate is accompanied by a slower detrapping process. Furthermore, there is a strong correlation between the electron density in the ZnO conduction band and the D_e during electron transport process, and the CdS shell formation reduces the exciton diffusion time (or distance) in the polymer phase to weaken its phase shift $\phi_n(\omega)$ effect on the electron transport. In the long run, our findings may provide theoretical guidance for fabricating and optimizing the HPSCs based on core/shell nanoarrays, and the model is expected to find extended applications to other core/shell nanorods based excitonic solar cells.

dx.doi.org/10.1021/jp509369n | J. Phys. Chem. C 2014, 118, 28462−28473

■ ASSOCIATED CONTENT

Supporting Information

ITO areas occupied by subdevices, weighted average of photocurrent densities, calculation of f_2 value, detailed solutions for the analytical expressions in MEH-PPV/CdS-ZnO-NA-U1 subdevice, additional calculated results for S_0, J–V, IPCE data, and IMVS results. This material is available free of charge via the Internet at http://pubs.acs.org.

■ AUTHOR INFORMATION

Corresponding Author

*Tel./Fax: 0086-551-65593171. E-mail: mtwang@ipp.ac.cn.

Notes

The authors declare no competing financial interest.

■ ACKNOWLEDGMENTS

This work was supported by the "100-Talent Program" of Chinese Academy of Sciences, the National Natural Science Foundation of China (11274307, 91333121, and 51202002), the Natural Science Foundation of Anhui Province (1308085ME70), and the President Foundation of Hefei Institute of Physical Sciences. We also acknowledge the referees involved for their generous advice on revision.

■ REFERENCES

(1) Saunders, B. R.; Turner, M. L. Nanoparticle-Polymer Photovoltaic Cells. *Adv. Colloid Interface Sci.* **2008**, *138*, 1–23.

(2) Huynh, W. U.; Dittmer, J. J.; Alivisatos, A. P. Hybrid Nanorod-Polymer Solar Cells. *Science* **2002**, *295*, 2425–2427.

(3) Beek, W. J. E.; Wienk, M. M.; Kemerink, M.; Yang, X. N.; Janssen, R. A. J. Hybrid Zinc Oxide Conjugated Polymer Bulk Heterojunction Solar Cells. *J. Phys. Chem. B* **2005**, *109*, 9505–9516.

(4) Beek, W. J. E.; Wienk, M. M.; Janssen, R. A. J. Hybrid Solar Cells from Regioregular Polythiophene and ZnO Nanoparticles. *Adv. Funct. Mater.* **2006**, *16*, 1112–1116.

(5) Günes, S.; Neugebauer, H.; Sariciftci, N. S. Conjugated Polymer-Based Organic Solar Cells. *Chem. Rev.* **2007**, *107*, 1324–1338.

(6) Hochbaum, A. I.; Yang, P. D. Semiconductor Nanowires for Energy Conversion. *Chem. Rev.* **2010**, *110*, 527–546.

(7) Weickert, J.; Dunbar, R. B.; Hesse, H. C.; Wiedemann, W.; Schmidt-Mende, L. Nanostructured Organic and Hybrid Solar Cells. *Adv. Mater.* **2011**, *23*, 1810–1828.

(8) Muskens, O. L.; Rivas, J. G.; Algra, R. E.; Bakkers, E.; Lagendijk, A. Design of Light Scattering in Nanowire Materials for Photovoltaic Applications. *Nano Lett.* **2008**, *8*, 2638–2642.

(9) Gonzalez-Valls, I.; Lira-Cantu, M. Vertically-Aligned Nanostructures of ZnO for Excitonic Solar Cells: A Review. *Energy Environ. Sci.* **2009**, *2*, 19–34.

(10) Ravirajan, P.; Peiró, A. M.; Nazeeruddin, M. K.; Graetzel, M.; Bradley, D. D. C.; Durrant, J. R.; Nelson, J. Hybrid Polymer/Zinc Oxide Photovoltaic Devices with Vertically Oriented ZnO Nanorods and an Amphiphilic Molecular Interface Layer. *J. Phys. Chem. B* **2006**, *110*, 7635–7639.

(11) Lin, Y.-Y.; Lee, Y.-Y.; Chang, L.; Wu, J.-J.; Chen, C.-W. The Influence of Interface Modifier on the Performance of Nanostructured ZnO/Polymer Hybrid Solar Cells. *Appl. Phys. Lett.* **2009**, *94*, 063308.

(12) Peiro, A. M.; Ravirajan, P.; Govender, K.; Boyle, D. S.; O'Brien, P.; Bradley, D. D. C.; Nelson, J.; Durrant, J. R. Hybrid Polymer/Metal Oxide Solar Cells Based on ZnO Columnar Structures. *J. Mater. Chem.* **2006**, *16*, 2088–2096.

(13) Olson, D. C.; Piris, J.; Collins, R. T.; Shaheen, S. E.; Ginley, D. S. Hybrid Photovoltaic Devices of Polymer and ZnO Nanofiber Composites. *Thin Solid Films* **2006**, *496*, 26–29.

(14) Olson, D. C.; Shaheen, S. E.; Collins, R. T.; Ginley, D. S. The Effect of Atmosphere and ZnO Morphology on the Performance of Hybrid Poly(3-hexylthiophene)/ZnO Nanofiber Photovoltaic Devices. *J. Phys. Chem. C* **2007**, *111*, 16670–16678.

(15) Bi, D.; Wu, F.; Qu, Q.; Yue, W.; Cui, Q.; Shen, W.; Chen, R.; Liu, C.; Qiu, Z.; Wang, M. Device Performance Related to Amphiphilic Modification at Charge Separation Interface in Hybrid Solar Cells with Vertically Aligned ZnO Nanorod Arrays. *J. Phys. Chem. C* **2011**, *115*, 3745–3752.

(16) Greene, L. E.; Law, M.; Yuhas, B. D.; Yang, P. ZnO–TiO_2 Core–Shell Nanorod/P3HT Solar Cells. *J. Phys. Chem. C* **2007**, *111*, 18451–18456.

(17) Wu, F.; Cui, Q.; Qiu, Z.; Liu, C.; Zhang, H.; Shen, W.; Wang, M. Improved Open-Circuit Voltage in Polymer/Oxide-Nanoarray Hybrid Solar Cells by Formation of Homogeneous Metal Oxide Core/Shell Structures. *ACS Appl. Mater. Interfaces* **2013**, *5*, 3246–3254.

(18) Cui, Q.; Liu, C.; Wu, F.; Yue, W.; Qiu, Z.; Zhang, H.; Gao, F.; Shen, W.; Wang, M. Performance Improvement in Polymer/ZnO Nanoarray Hybrid Solar Cells by Formation of ZnO/CdS-Core/Shell Heterostructures. *J. Phys. Chem. C* **2013**, *117*, 5626–5637.

(19) Lippens, P. E.; Lannoo, M. Calculation of the Band-Gap for Small CdS and ZnS Crystallites. *Phys. Rev. B* **1989**, *39*, 10935–10942.

(20) Mora-Seró, I.; Likodimos, V.; Giménez, S.; Martínez-Ferrero, E.; Albero, J.; Palomares, E.; Kontos, A. G.; Falaras, P.; Bisquert, J. Fast Regeneration of CdSe Quantum Dots by Ru Dye in Sensitized TiO_2 Electrodes. *J. Phys. Chem. C* **2010**, *114*, 6755–6761.

(21) Shen, H.; Lin, H.; Liu, Y.; Li, J.; Oron, D. Study of Quantum Dot/Inorganic Layer/Dye Molecule Sandwich Structure for Electrochemical Solar Cells. *J. Phys. Chem. C* **2012**, *116*, 15185–15191.

(22) Bredas, J. L.; Norton, J. E.; Cornil, J.; Coropceanu, V. Molecular Understanding of Organic Solar Cells: The Challenges. *Acc. Chem. Res.* **2009**, *42*, 1691–1699.

(23) Nelson, J.; Kwiatkowski, J. J.; Kirkpatrick, J.; Frost, J. M. Modeling Charge Transport in Organic Photovoltaic Materials. *Acc. Chem. Res.* **2009**, *42*, 1768–1778.

(24) Zhu, X. Y.; Yang, Q.; Muntwiler, M. Charge-Transfer Excitons at Organic Semiconductor Surfaces and Interfaces. *Acc. Chem. Res.* **2009**, *42*, 1779–1787.

(25) Po, R.; Maggini, M.; Camaioni, N. Polymer Solar Cells: Recent Approaches and Achievements. *J. Phys. Chem. C* **2010**, *114*, 695–706.

(26) Dloczik, L.; Ileperuma, O.; Lauermann, I.; Peter, L. M.; Ponomarev, E. A.; Redmond, G.; Shaw, N. J.; Uhlendorf, I. Dynamic Response of Dye-Sensitized Nanocrystalline Solar Cells: Characterization by Intensity-Modulated Photocurrent Spectroscopy. *J. Phys. Chem. B* **1997**, *101*, 10281–10289.

(27) Zhang, D. S.; Yoshida, T.; Oekermann, T.; Furuta, K.; Minoura, H. Room-Temperature Synthesis of Porous Nanoparticulate TiO_2 Films for Flexible Dye-Sensitized Solar Cells. *Adv. Funct. Mater.* **2006**, *16*, 1228–1234.

(28) Dunn, H. K.; Peter, L. M. How Efficient Is Electron Collection in Dye-Sensitized Solar Cells? Comparison of Different Dynamic Methods for the Determination of the Electron Diffusion Length. *J. Phys. Chem. C* **2009**, *113*, 4726–4731.

(29) Chen, C.; Wang, M. T.; Wang, K. J. Characterization of Polymer/TiO_2 Photovoltaic Cells by Intensity Modulated Photocurrent Spectroscopy. *J. Phys. Chem. C* **2009**, *113*, 1624–1631.

(30) Chen, C.; Peng, R. X.; Wu, H.; Wang, M. T. Electric Field Effects on Charge Transport in Polymer/TiO_2 Photovoltaic Cells Investigated by Intensity Modulated Photocurrent Spectroscopy. *J. Phys. Chem. C* **2009**, *113*, 12608–12614.

(31) Wu, F.; Shen, W.; Cui, Q.; Bi, D.; Yue, W.; Qu, Q.; Wang, M. Dynamic Characterization of Hybrid Solar Cells Based on Polymer and Aligned ZnO Nanorods by Intensity Modulated Photocurrent Spectroscopy. *J. Phys. Chem. C* **2010**, *114*, 20225–20235.

(32) Balkanski, M.; Waldron, R. D. Internal Photoeffect and Exciton Diffusion in Cadmium and Zinc Sulfides. *Phys. Rev.* **1958**, *112*, 123–135.

(33) Botev, I. New Conception of Bouguer–Lambert–Beer Law. *Fresenius' Z. Anal. Chem.* **1979**, *297*, 419–419.

(34) Markov, D. E.; Tanase, C.; Blom, P. W. M.; Wildeman, J. Simultaneous Enhancement of Charge Transport and Exciton

Diffusion in Poly(*p*-phenylene vinylene) Derivatives. *Phys. Rev. B* **2005**, *72*, 045217.
(35) Lewis, A. J.; Ruseckas, A.; Gaudin, O. P. M.; Webster, G. R.; Burn, P. L.; Samuel, I. D. W. Singlet Exciton Diffusion in MEH-PPV Films Studied by Exciton−Exciton Annihilation. *Org. Electron.* **2006**, *7*, 452−456.
(36) Greene, L. E.; Law, M.; Tan, D. H.; Montano, M.; Goldberger, J.; Somorjai, G.; Yang, P. General Route to Vertical ZnO Nanowire Arrays Using Textured ZnO Seeds. *Nano Lett.* **2005**, *5*, 1231−1236.
(37) Yu, G.; Gao, J.; Hummelen, J. C.; Wudl, F.; Heeger, A. J. Polymer Photovoltaic Cells: Enhanced Efficiencies via a Network of Internal Donor-Acceptor Heterojunctions. *Science* **1995**, *270*, 1789−1791.
(38) Halls, J. J. M.; Walsh, C. A.; Greenham, N. C.; Marseglia, E. A.; Friend, R. H.; Moratti, S. C.; Holmes, A. B. Efficient Photodiodes from Interpenetrating Polymer Networks. *Nature* **1995**, *376*, 498−500.
(39) Peter, L. M. Dynamic Aspects of Semiconductor Photoelectrochemistry. *Chem. Rev.* **1990**, *90*, 753−769.
(40) Tennakone, K.; Jayaweera, P. V. V; Bandaranayake, P. K. M. Dye-Sensitized Photoelectrochemical and Solid-State Solar Cells: Charge Separation, Transport and Recombination Mechanisms. *J. Photochem. Photobiol., A* **2003**, *158*, 125−130.
(41) Quintana, M.; Edvinsson, T.; Hagfeldt, A.; Boschloo, G. Comparison of Dye-Sensitized ZnO and TiO_2 Solar Cells: Studies of Charge Transport and Carrier Lifetime. *J. Phys. Chem. C* **2007**, *111*, 1035−1041.
(42) Salafsky, J. S. Exciton Dissociation, Charge Transport, and Recombination in Ultrathin, Conjugated Polymer-TiO_2 Nanocrystal Intermixed Composites. *Phys. Rev. B* **1999**, *59*, 10885−10894.
(43) Gregg, B. A.; Hanna, M. C. Comparing Organic to Inorganic Photovoltaic Cells: Theory, Experiment, and Simulation. *J. Appl. Phys.* **2003**, *93*, 3605−3614.
(44) Savenije, T. J.; Warman, J. M.; Goossens, A. Visible Light Sensitisation of Titanium Dioxide Using a Phenylene Vinylene Polymer. *Chem. Phys. Lett.* **1998**, *287*, 148−153.
(45) Hotchandani, S.; Kamat, P. V. Charge-Transfer Processes in Coupled Semiconductor Systems. Photochemistry and Photoelectrochemistry of the Colloidal Cadmium Sulfide-Zinc Oxide System. *J. Phys. Chem.* **1992**, *96*, 6834−6839.
(46) Song, X.; Yu, X.-L.; Xie, Y.; Sun, J.; Ling, T.; Du, X.-W. Improving Charge Separation of Solar Cells by the Co-Sensitization of CdS Quantum Dots and Dye. *Semicond. Sci. Technol.* **2010**, *25*, 095014.
(47) Franco, G.; Peter, L. M.; Ponomarev, E. A. Detection of Inhomogeneous Dye Distribution in Dye Sensitised Nanocrystalline Solar Cells by Intensity Modulated Photocurrent Spectroscopy (IMPS). *Electrochem. Commun.* **1999**, *1*, 61−64.
(48) Koynov, K.; Bahtiar, A.; Ahn, T.; Bubeck, C. Molecular Weight Dependence of Birefringence of Thin Films of the Conjugated Polymer Poly[2-methoxy-5-(2′-ethyl-hexyloxy)-1,4-phenylenevinylene]. *Appl. Phys. Lett.* **2004**, *84*, 3792−3794.
(49) Raut, B. T.; Godse, P. R.; Pawar, S. G.; Chougule, M. A.; Patil, V. B. Development of Nanostructured CdS Sensor for H_2S Recognition: Structural and Physical Characterization. *J. Mater. Sci.: Mater. Electron.* **2012**, *23*, 956−963.
(50) Fisher, A. C.; Peter, L. M.; Ponomarev, E. A.; Walker, A. B.; Wijayantha, K. G. U. Intensity Dependence of the Back Reaction and Transport of Electrons in Dye-Sensitized Nanocrystalline TiO_2 Solar Cells. *J. Phys. Chem. B* **2000**, *104*, 949−958.
(51) Knupfer, M. Exciton Binding Energies in Organic Semiconductors. *Appl. Phys. A: Mater. Sci. Process.* **2003**, *77*, 623−626.
(52) de Jongh, P. E.; Vanmaekelbergh, D. Trap-Limited Electronic Transport in Assemblies of Nanometer-Size TiO_2 Particles. *Phys. Rev. Lett.* **1996**, *77*, 3427−3430.
(53) Vanmaekelbergh, D.; de Jongh, P. E. Electron Transport in Disordered Semiconductors Studied by a Small Harmonic Modulation of the Steady State. *Phys. Rev. B* **2000**, *61*, 4699−4704.
(54) Peter, L. M.; Wijayantha, K. G. U. Intensity Dependence of the Electron Diffusion Length in Dye-Sensitised Nanocrystalline TiO_2 Photovoltaic Cells. *Electrochem. Commun.* **1999**, *1*, 576−580.
(55) Peter, L. M.; Wijayantha, K. G. U. Electron Transport and Back Reaction in Dye Sensitized Nanocrystalline Photovoltaic Cells. *Electrochim. Acta* **2000**, *45*, 4543−4551.
(56) Bisquert, J.; Vikhrenko, V. S. Interpretation of the Time Constants Measured by Kinetic Techniques in Nanostructured Semiconductor Electrodes and Dye-Sensitized Solar Cells. *J. Phys. Chem. B* **2004**, *108*, 2313−2322.
(57) Peter, L. M. Dye-Sensitized Nanocrystalline Solar Cells. *Phys. Chem. Chem. Phys.* **2007**, *9*, 2630−2642.
(58) Oekermann, T.; Zhang, D.; Yoshida, T.; Minoura, H. Electron Transport and Back Reaction in Nanocrystalline TiO_2 Films Prepared by Hydrothermal Crystallization. *J. Phys. Chem. B* **2004**, *108*, 2227−2235.